Hamburger Beiträge
zur Angewandten Mathematik

A partitioned approach for adjoint shape optimization in fluid-structure interaction

J. P. Heners, L. Radtke, M. Hinze, A. Düster

Nr. 2016-22
September 2016

Noname manuscript No.
(will be inserted by the editor)

A partitioned approach for adjoint shape optimization in fluid-structure interaction

J.P. Heners · L. Radtke · M. Hinze · A. Düster

Received: date / Accepted: date

Zusammenfassung Based on the coupled problem of time-dependent fluid-structure interaction, equations for an appropriate adjoint problem are derived by the consequent use of the formal Lagrange calculus. Solutions of both primal and adjoint equations are computed in a partitioned fashion and enable the formulation of a surface sensitivity. This sensitivity is used in the context of a steepest descent algorithm for the computation of the required gradient of an appropriate cost functional. The efficiency of the developed optimization approach is demonstrated by minimization of the pressure drop in a simple two-dimensional channel flow and in a ducted blood-flow of a vascular artery.

Schlüsselwörter Fluid-Structure Interaction · Adjoint Shape Optimization · Adjoint FSI Optimization · Optimal Control of Fluid-Structure Interaction

1 Introduction

The growing amount of available computational capacities and the associated possibilities to consider mutual dependencies between fluid loads and structure deformations lead to an increase in the impact of applications considering fluid-structure interaction (FSI) in engineering, physics and health sciences. With rising fluid loads and deformations of the structure respectively, scientists and engineers face an increasing demand for considering interactions between fluids and structures. Common examples of fluid dynamic design tasks are fluttering of aircraft wings [1] and turbine blades [2], deformations of rudder

J.P. Heners
first address
Tel.: +123-45-678910
Fax: +123-45-678910
E-Mail: fauthor@example.com

S. Author
second address

constructions or sloshing loads on the hull of a ship. In this paper, we focus on the computation of vascular blood flows, where periodic pressure loads in conjunction with the hyperelastic walls of an artery result in large deformations of the flow channel, which cause significant mutual coupling between both the flow field and the deformation of the artery.

Furthermore, the growing available computer performance arises increasingly questions of how to go beyond pure prediction of system behaviour and how to challenge the modification of specific design parameters to improve the system performance. In this context, adjoint shape optimization has become quite a popular approach in the last decade, mainly due to its low numerical costs in terms of numerical effort and computational time. In the past, a lot of works focussed on the optimization of purely fluid dynamic design tasks (see, e.g. [3][4][5][6][7][8][9]) neglecting the dependencies of flow fields and involved structures which is sufficient in many engineering applications. In [10], the coupling of flow field and energy transport due to heat transfer is considered in the adjoint optimization approach by referring to an appropriate system consisting of energy and Reynolds-averaged Navier-Stokes (RANS) equations.

An approach considering the dependencies between fluid and structure in the context of an adjoint optimization framework can be found in [11], where the formulated optimization strategy is applied to the dynamic steering of system behaviour controlled by a force acting on the structure. The derivative of the cost functional is computed from both primal and adjoint solutions and is used in the context of a steepest descent algorithm. Both primal and adjoint (dual) FSI-problems are solved simultaneously by usage of proper Finite Element (FE) formulations during the solution of the governing partial differential equations (PDE) for fluid and structure respectively.

Similar to [11], in this paper we propose a partitioned optimization strategy for time-dependent FSI-applications based on adjoint methods to compute the gradient of a cost functional to be minimized in the framework of a steepest descent algorithm. In contrast to [11], the control parameter in this work is the shape of the involved structure. In particular, we are interested in affecting the flow behaviour of an artificial blood vessel by variation of its shape to find optimal conditions for future patients and their surgeons.

The optimization approach chosen in this work is illustrated in Figure 1 and is based on an iterative application of a steepest descent algorithm as described in [6] for common adjoint design tasks. Starting with an initial shape configuration u^k, the first step in computing the required gradient consists according to Figure 1 in solving the time-dependent FSI-problem. As shown in Figure 1, the solution of the appropriate adjoint system is then calculated by referring to required information from the primal solution process in a second step.

According to Figure 1, knowledge of both primal and adjoint state of the system allows in a third step for an efficient computation of the derivative of the corresponding cost functional which can in the context of shape design be identified with a surface sensitivity. The required gradient (in [6] also called Sobolev gradient) is then obtained by taking advantage of the Riesz represen-

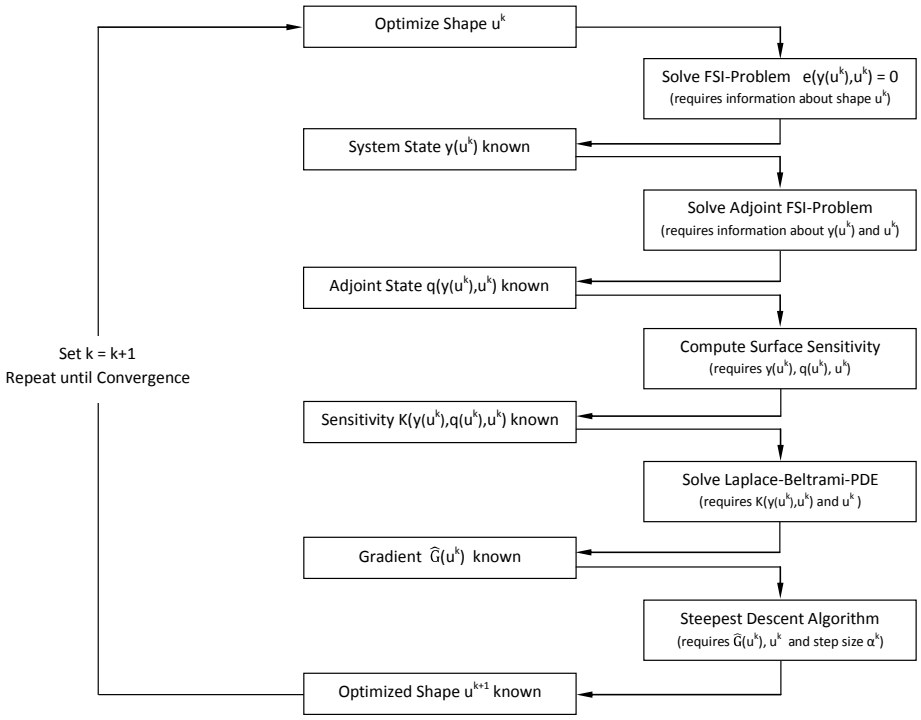

Abb. 1 Adjoint-based optimization framework in the context of a steepest descent algorithm (see, e.g. [6]).

tation theorem leading to an additional PDE to be solved. In this situation, the resulting Laplace-Beltrami PDE is solved in a fourth step by usage of the sensitivity information calculated before. The initial shape geometry u^k is then modified according to the computed gradient distribution in the framework of a steepest descent algorithm and the whole optimization process is repeated iteratively.

In the context of this paper, we focus on the minimization of the pressure drop in the considered model artery, the derivation of the required adjoint time-dependent FSI-problem and the computation of a smooth gradient using a surface sensitivity influenced by both primal and adjoint solutions. The paper is outlined as follows. First, we briefly discuss in section 2 the derivation of adjoint equations relating to the well known time dependent FSI-problem as well as their numerical properties in the context of a partitioned solution approach. In section 3, we present an approach to compute derivative and gradient of an arbitrary cost functional based on the knowledge of primal and adjoint solutions. Finally, we show the capability of the developed optimization strategy by two examples in section 4 and draw some closing conclusions in section 5.

2 Primal and adjoint FSI-problem

This section presents the derivation of the adjoint FSI-Problem and its characteristic properties in terms of a partitioned solution framework. Derivations of both adjoint equations and boundary conditions are presented after a brief recapitulation of the underlying FSI-problem in Arbitrary Lagrangian-Eulerian (ALE) formulation. The whole work assumes the fluids to be of incompressible Newtonian nature and allows for large deformations of the involved structures which are modelled as thin-walled anisotropic three-dimensional hyperelastic continua based on the St. Venant-Kirchhoff material model.

2.1 Primal FSI-problem in ALE-formulation

The time-dependent FSI-problem considered in this work is given in a residual form by equations (1 - 4). The time-dependent physical domain $\Omega^\tau := (\Omega \times T)$ herein is separated in a fluid domain $\Omega_f^\tau := (\Omega_f \times T)$ and a structural domain $\Omega_s^\tau := (\Omega_s \times T)$ connected by an interface boundary Γ_{IF}^τ as illustrated in Figure 2.

$$\mathrm{R}_i = \frac{\partial v_i}{\partial t} + \big(v - v_m\big)_j \frac{\partial v_i}{\partial x_j} + \frac{\partial}{\partial x_j}\left[\overline{p}\,\delta_{ij} - 2\,\nu\,S_{ij}\right] = 0 \quad \text{in} \quad \Omega_f^\tau \tag{1}$$

$$\mathrm{Q} = \frac{\partial v_i}{\partial x_i} = 0 \quad \text{in} \quad \Omega_f^\tau \tag{2}$$

$$\mathrm{B}_i = \rho_s \frac{\partial^2 d_i}{\partial t^2} - \frac{\partial \mathrm{P}_{iJ}}{\partial X_J} - \rho_s \mathrm{b}_i = 0 \quad \text{in} \quad \Omega_{s,o}^\tau \tag{3}$$

$$\mathrm{C}_i = v_i - \dot{d}_i = 0 \quad \text{on} \quad \Gamma_{\text{IF}}^\tau \tag{4}$$

Since we are only considering incompressible Newtonian fluids without volume loads, the governing equations for fluid velocity v_i and specific fluid pressure $\overline{p} = \frac{p}{\rho_f}$ are given by the incompressible Navier-Stokes equations, which are momentum equations R_i (1) and continuity equation Q (2), both formulated in an ALE-framework. Here, v_m is the velocity of the fluid domain Ω_f^τ, and ρ_f and ν denote the density and kinematic viscosity of the fluid. Furthermore, S_{ij} defines the rate of strain tensor $S_{ij} = \frac{1}{2}\big(\frac{\partial v_i}{\partial x_j} + \frac{\partial v_j}{\partial x_i}\big)$ of the fluid velocity v_i.

The governing structural mechanics equations (3) for the structural displacement d_i are given by the balance of momentum described in terms of the reference configuration $\Omega_{s,o}$ of the structure. In eq. (3), ρ_s defines the density of the structure, P_{iJ} the first Piola-Kirchhoff stress tensor and b_i the vector of specific body forces. The associated constitutive equations are based on a hyperelastic behaviour defining the stresses as $\mathrm{P}_{iJ} = F_{iI}\mathbb{S}_{IJ}$ with $\mathbb{S}_{IJ} = \lambda\delta_{IJ}E_{IJ} + 2\mu E_{IJ}$ being the second Piola-Kirchhoff stress tensor and $F_{iI} = \frac{\partial x_i}{\partial X_I} = \delta_{iI} + \frac{\partial d_i}{\partial X_I}$ being the deformation gradient. In the definition of

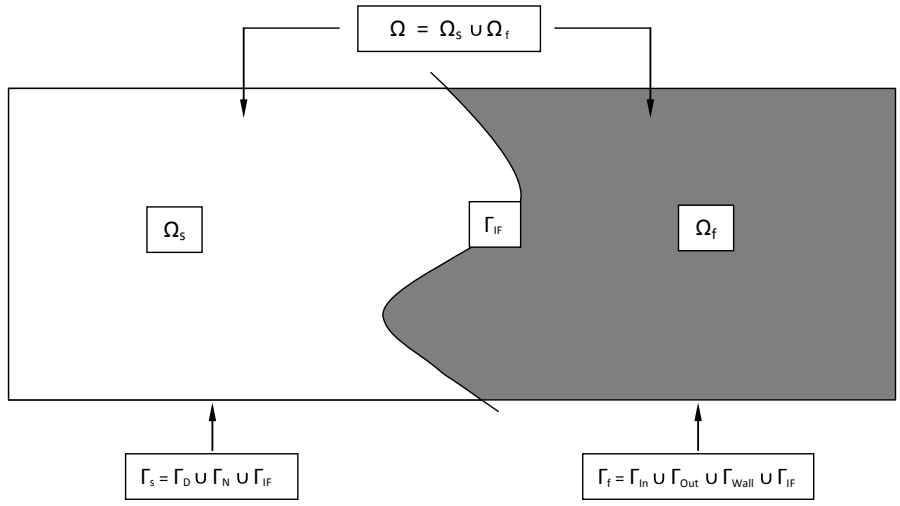

Abb. 2 Spatial domain in the considered FSI-framework including the structural subdomain Ω_s (white) and the fluid subdomain Ω_f (grey).

the second Piola-Kirchhoff stress tensor $\mathbb{S}_{IJ}$, E_{IJ} denotes the Green-Lagrange strain tensor defined by $E_{IJ} = \frac{1}{2}(F_{iI}F_{iJ} - \delta_{IJ})$ with Lamé constants λ and μ.

To ensure proper coupling properties at the FSI-interface $\Gamma_{\mathrm{IF}}^{\tau} := (\Gamma_{\mathrm{IF}} \times T)$, we postulate fluid velocity v_i and stuctural velocity $\dot{d}_i$ to be equal on the interaction boundary $\Gamma_{\mathrm{IF}}^{\tau}$, which yields the latter constraint (4). Furthermore, we require fluid and structural tractions to be in equilibrium at the fluid-structure interface $\Gamma_{\mathrm{IF}}^{\tau}$ which can be achieved by an equality of the associated test functions $\delta v_i = \delta d_i$ of fluid and structure, respectively at the interface (see e.g. [12][13]).

2.2 Optimal control problem and PDE constraints

In this subsection we provide a formulation of the considered optimal control problem and of a proper Lagrange functional $\mathcal{L}$ by introducing suitable Lagrange multipliers. Based on this Lagrange functional, an adjoint FSI-problem is derived in the next subsection which allows us to compute a surface sensitivity as a function of the chosen cost functional as well as of solutions of the associated primal and adjoint systems. A common form of an optimization problem concerned by a PDE-constraint $e(y, u) = 0$ can be stated as

$$\min_{u \in U_{\mathrm{ad}}} \quad J(y, u) \qquad \text{s.t.} \quad e(y, u) = 0 \quad . \tag{5}$$

This can be interpreted as follows. Find the control parameter u in the set of admissible control states U_{ad}, that minimizes the cost functional J (which

is a function of the state variable y and the control parameter u), subject to the PDE-constraint $e(y,u) = 0$ (which is again a function of state variable y and control parameter u). In our case, the control parameter u is the shape of the structure, since in terms of shape optimization we want to affect the performance of an artificial artery just by variation of its shape. The set of admissable controls U_{ad} can be affected by both technical and theoretical constraints. From the theoretical point of view, we require at least a continuous and steady formulation of u relying on a feasible parametrization of the shape. Furthermore, the set of admissable controls can be restricted additionally by technical aspects (e.g. fixed positions of inlet and outlet or constraints in the dimensions of the assembly).

Since the considered FSI-problem defined by eq. (1 - 4) is completely determined by knowledge of fluid velocity v_i, fluid pressure $\overline{p}$ and structural displacements d_i, the state of the considered system can be described by

$$y(u) = \left\{ \begin{pmatrix} v_{i(\mathrm{u})} \\ \overline{p}_{\,(\mathrm{u})} \\ d_{i(\mathrm{u})} \end{pmatrix} \right\} \in \left(Y_{\mathrm{ad}} \right) \quad , \tag{6}$$

where $Y_{\mathrm{ad}} = (V_{\mathrm{ad}}\ P_{\mathrm{ad}}\ S_{\mathrm{ad}})^T$ is the set of admissible states of fluid velocities v_i, specific fluid pressures $\overline{p}$ and structural displacements d_i. Since changes in the shape u cause changes in both flow and displacement field, the state variable y in eq. (6) can be interpreted as a function of u. Here, we assume that there is a unique solution to the physical problem given by eq. (1)-(4) for all shapes $u \in U_{\mathrm{ad}}$ of the fluid-structure interface Γ_{IF}. Therefore, we can formulate an equivalent reduced cost functional

$$\widehat{J} := \widehat{J}(u) : \qquad H^1(\Gamma, \mathbb{R}) \longrightarrow \mathbb{R} \tag{7}$$

being just a function of the control parameter u. Here, $H^1(\Gamma, \mathbb{R}^3)$ denotes the associated Sobolev space $W^{1,2}(\Gamma, \mathbb{R}^3)$. Focussing on FSI-applications, the PDE-constraint $e(y,u) = 0$ is then given by the residual formulation of the primal FSI-problem in eq. (1 - 4), i.e.

$$e(y,u) = \left\{ \begin{array}{lll} \mathrm{R}_i = \frac{\partial v_i}{\partial t} + (v - v_m)_j \frac{\partial v_i}{\partial x_j} + \frac{\partial}{\partial x_j}\left[\overline{p} \cdot \delta_{ij} - 2\,\nu\, S_{ij}\right] & \text{in} & \Omega_f^\tau \\ \mathrm{Q} = \frac{\partial v_i}{\partial x_i} & \text{in} & \Omega_f^\tau \\ \mathrm{B}_i = \rho_s \frac{\partial^2 d_i}{\partial t^2} - \frac{\partial \mathrm{P}_{iJ}}{\partial X_J} - \rho_s \mathrm{b}_i & \text{in} & \Omega_{s,o}^\tau \\ \mathrm{C}_i = v_i - \dot{d}_i & \text{on} & \Gamma_{\mathrm{IF}}^\tau \end{array} \right\} = 0 \quad . \tag{8}$$

The definition of the constrained optimization problem in eq. (5) allows now the use of the formal Lagrange principle to eliminate the constraints by introducing proper Lagrange multipliers as proposed by [8]. In this context, we

formulate in eq. (9) a Langrange functional $\mathcal{L}$ using a continuous formulation of Lagrange multipliers $\widehat{v}_i$, $\widehat{p}$, $\widehat{d}_i$ and $\widehat{\kappa}_i$ for the momentum equations R_i (1), continuity equation Q (2), structural mechanics equations B_i (3) and the coupling constraint C_i (4), respectively.

$$\mathcal{L} := J + \int\limits_{(\Omega_f \times T)} \widehat{v}_i \, \mathrm{R}_i - \widehat{p} \, \mathrm{Q} \; d\Omega^\tau + \int\limits_{(\Omega_{s,o} \times T)} \widehat{d}_i \, \mathrm{B}_i \, d\Omega_o^\tau + \int\limits_{(\Gamma_{\mathrm{IF}} \times T)} \widehat{\kappa}_i \, \mathrm{C}_i \; d\Gamma^\tau \quad (9)$$

Since the pursued partitioned solution approach demands a description of the structure in terms of its initial shape, we consider in the following part of this work the constraint B_i in its reference configuration $\Omega_{s,o}$. According to the formal Lagrange principle, the optimal control problem (5) is now equivalent to the minimization problem

$$\min \; \mathcal{L}(v_i, \overline{p}, d_i, u, \widehat{v}_i, \widehat{p}, \widehat{d}_i, \widehat{\kappa}_i) \, , \qquad y \text{ unconstrained}, \; u \in U_{ad} \quad , \qquad (10)$$

without any restrictions to the state variable y [14]. From a physical point of view, it is obvious that we require u being in the interiour of the space of admissable controls U_{ad} and keeping in mind that for a minimum of the Lagrange functional (9) the total derivative $\delta\mathcal{L}$ vanishes, we obtain the following optimality conditions:

$$\begin{aligned}
\delta_{\overline{p}}\mathcal{L} \cdot \delta\overline{p} &= 0 \quad \forall \, \delta\overline{p} \in P_{\mathrm{ad}} && (11)\\
\delta_{v}\mathcal{L} \cdot \delta v_i &= 0 \quad \forall \, \delta v_i \in V_{\mathrm{ad}} && (12)\\
\delta_{d}\mathcal{L} \cdot \delta d_i &= 0 \quad \forall \, \delta d_i \in S_{\mathrm{ad}} && (13)\\
\delta_{u}\mathcal{L} \cdot \delta u &= 0 \quad \forall \, \delta u \in U_{\mathrm{ad}} \quad . && (14)
\end{aligned}$$

2.3 Adjoint FSI-problem in ALE-formulation

The adjoint FSI-system can now be obtained by exploiting the optimality conditions listed above. Every optimality condition leads to a PDE for the introduced Lagrange multipliers in eq. (9) and contributes to the requested adjoint FSI-problem. Assuming that the considered cost functional J can be separated into contributions over the boundary Γ^τ and the interior of the physical domain Ω^τ as proposed in [7]

$$J = \int\limits_{(\Gamma \times T)} j_\Gamma \, d\Gamma^\tau + \int\limits_{(\Omega \times T)} j_\Omega \, d\Omega^\tau \quad , \qquad (15)$$

we obtain from the first optimality condition (11) after computation of the Fréchet derivative $\delta_{\overline{p}}\mathcal{L}$ and application of integration by parts

$$\delta_{\overline{p}}\mathcal{L}\cdot\delta\overline{p} = \int\limits_{(\Omega\times T)} \left(\delta\overline{p}\right)\left\{\frac{\partial j_\Omega}{\partial p} - \frac{\partial\widehat{v}_i}{\partial x_i}\right\} d\Omega^\tau \;+\int\limits_{(\Gamma\times T)}\left(\delta\overline{p}\right)\left\{\widehat{v}_n + \frac{\partial j_\Gamma}{\partial p}\right\} d\Gamma^\tau$$
$$\stackrel{!}{=} \quad 0 \quad \forall\ \delta\overline{p}\in P_{\mathrm{ad}} \quad . \tag{16}$$

Since eq. (16) holds for all test functions $\delta\overline{p}$ and both components are defined over different domains, being the interior of the physical domain Ω^τ and its boundary Γ^τ, eq. (16) can only be satisfied if each integrand vanishes. So we conclude from the first optimality condition via pressure variation of the Lagrange functional (9) the following constraints for the Lagrange multiplier $\widehat{v}_i$

$$\frac{\partial\widehat{v}_i}{\partial x_i} = \frac{\partial j_\Omega}{\partial p} \qquad \text{in} \qquad (\Omega_f\times T) \tag{17}$$
$$\widehat{v}_n = -\frac{\partial j_\Gamma}{\partial p} \qquad \text{on} \qquad (\Gamma_{\mathrm{In}}\times T) \quad . \tag{18}$$

Equation (17) is also called "adjoint continuity equation" due to its analogy to the primal continuity equation (2). In the context of the adjoint solution framework, eq. (18) is used as a boundary condition for the Lagrange multiplier $\widehat{v}_i$ over the inlet Γ_{In} of the fluid domain Ω_f.

In the next step, we derive analogously adjoint momentum equations from the second optimality condition $\delta_v\mathcal{L}\cdot\delta v_i = 0$ by variation of velocity in the Lagrange functional (9). Again we use a continuous formulation of the cost fuctional as shown in eq. (15) and conclude by computation of the Fréchet derivative $\delta_v\mathcal{L}$ and application of integration by parts

$$\begin{aligned}
\delta_v\mathcal{L}\cdot\delta v_i = \quad & \delta_v J\cdot\delta v_i \\
& + \int\limits_{(\Omega\times T)}\left(\delta v_i\right)\left\{ - \frac{\partial\widehat{v}_i}{\partial t} - \left(v - v_m\right)_j \frac{\partial\widehat{v}_i}{\partial x_j} - v_j\,\frac{\partial\widehat{v}_j}{\partial x_i} + \frac{\partial\widehat{p}}{\partial x_i} - \frac{\partial}{\partial x_j}\left(2\nu\,\widehat{S}_{ij}\right)\right\} d\Omega^\tau \\
& + \oint\limits_{(\partial\Omega\times T)} \left(\delta v_i\right)\left\{ v_j\,n_j\,\widehat{v}_i + v_j\,n_i\,\widehat{v}_j - v_{m,j}\,n_j\,\widehat{v}_i + \nu\frac{\partial\widehat{v}_i}{\partial x_j}\,n_j - \widehat{p}\,n_i\right\} d\Gamma^\tau \\
& + \int\limits_{\Omega_f}\widehat{v}_i\,\left(\delta v_i\right)\,d\Omega\,\Big|_{t=0}^{t=t_{end}} - \oint\limits_{(\partial\Omega\times T)}\nu\,\widehat{v}_j\,\frac{\partial\left(\delta v_j\right)}{\partial x_i}\;n_i d\Gamma^\tau + \int\limits_{(\Gamma_{\mathrm{IF}}\times T)}\widehat{\kappa}_i\,\left(\delta v_i\right)\;d\Gamma^\tau \\
& \stackrel{!}{=} 0 \qquad \forall\ \delta v_i\in V_{\mathrm{ad}} \quad .
\end{aligned} \tag{19}$$

During the derivation of eq. (19), we make use of the principle of a "frozen fluid domain velocity" (see, e.g. [11]), which expects in a first approach the velocity of the time-dependent fluid domain $\Omega_f^\tau = (\Omega_f(t)\times T)$ to be approximately constant, that is $\delta_v(v_m) = 0$. In eq. (19), $\widehat{S}_{ij}$ defines the adjoint rate of strain

tensor $\widehat{S}_{ij} = \frac{1}{2}\left(\frac{\partial \widehat{v}_i}{\partial x_j} + \frac{\partial \widehat{v}_j}{\partial x_i}\right)$ of the Lagrange multiplier $\widehat{v}_i$. As before, the integrands in eq. (19) have to vanish due to the varying integral domains which leads us to the following set of equations for the Lagrange multipliers $\widehat{v}_i$ and $\widehat{p}$.

$$
\begin{aligned}
&-\frac{\partial \widehat{v}_i}{\partial t} - \left(v - v_m\right)_j \frac{\partial \widehat{v}_i}{\partial x_j} - v_j \frac{\partial \widehat{v}_j}{\partial x_i} \\
&\qquad + \frac{\partial}{\partial x_j}\left\{\widehat{p}\,\delta_{ij} - 2\nu\,\widehat{S}_{ij}\right\} + \frac{\partial j_{\Omega_f}}{\partial v_i} = 0 \qquad \text{in} \quad (\Omega_f \times T) \qquad (20)\\
&\qquad\qquad \widehat{v}_{i,(t=t_{\text{end}})} = 0 \qquad \text{in} \quad (\Omega_f) \qquad (21)\\
&\qquad\qquad \widehat{v}_t = 0 \qquad \text{on} \quad (\Gamma_{\text{In}} \times T) \qquad (22)\\
&\qquad\qquad \frac{\partial \widehat{p}}{\partial x_i}\, n_i = 0 \qquad \text{on} \quad (\Gamma_{\text{In}} \times T) \qquad (23)\\
&\qquad v_j\,\widehat{v}_j + v_n\,\widehat{v}_n + \nu\,\frac{\partial \widehat{v}_n}{\partial n} + \frac{\partial j_\Gamma}{\partial v_n} = \widehat{p} \qquad \text{on} \quad (\Gamma_{\text{Out}} \times T) \qquad (24)\\
&\qquad\qquad v_n\,\widehat{v}_t + \nu\,\frac{\partial \widehat{v}_t}{\partial n} + \frac{\partial j_\Gamma}{\partial v_t} = 0 \qquad \text{on} \quad (\Gamma_{\text{Out}} \times T) \qquad (25)
\end{aligned}
$$

Here, the boundary component Γ_{Out} stands for the outlet part of the fluid domain Ω_f. The PDE (20) describing the behaviour of the Lagrange multipliers $\widehat{v}_i$ and $\widehat{p}$ is very similar to the primal momentum equation (1) and is therefore called "adjoint momentum equation". As the primal momentum equation (1) before, the adjoint momentum equation (20) is formulated in an ALE-framework by referring to the primal mesh velocity v_m in the adjoint convection term $\{-\left(v - v_m\right)_j \frac{\partial \widehat{v}_i}{\partial x_j}\}$.

The set of PDEs defined by eq. (17) and (20) is denoted as "adjoint Navier-Stokes equations" and determines the Lagrange multipliers $\widehat{v}_i$ and $\widehat{p}$ completely. Since in the Lagrangian sense adjoint state variables and introduced Lagrange multipliers are equivalent and since the structures of primal and adjoint equations are very similar, we call the Lagrange multipliers $\widehat{v}_i$ and $\widehat{p}$ "adjoint velocity" and "adjoint pressure" respectively. In eq. (20) - (25), the terms defined over the FSI-interface Γ_{IF} have not been included so far, since they will be either used to derive an adjoint interface condition at the end of this subsection or contribute to the desired surface sensitivity as discussed in section 3.

From the third optimality condition (13) we now derive the missing information about the remaining Lagrange multiplier $\widehat{d}_i$. We proceed as before by computing the required Fréchet derivative $\delta_d \mathcal{L}$ and by the subsequent use of integration by parts in terms of the reference configuration Ω_o.

$$
\begin{aligned}
\delta_d \mathcal{L} \cdot \delta d_i = & \int\limits_{(\Omega_{0,s} \times T)} \rho_s \left(\delta d_i\right) \frac{\partial^2 \widehat{d}_i}{\partial t^2} + \frac{\partial \widehat{d}_i}{\partial X_J} \, \mathrm{D}_{iJkL} \, \frac{\partial \left(\delta d_i\right)}{\partial X_I} + \frac{\partial j_{\Omega_s}}{\partial d_i} \left(\delta d_i\right) \, d\Omega_0^\tau \\
& + \int\limits_{(\Omega_{0,s})} \rho_s \left(\widehat{d}_i \, \frac{\partial \left(\delta d_i\right)}{\partial t} - \left(\delta d_i\right) \frac{\partial \widehat{d}_i}{\partial t} \right) d\Omega_0 \Bigg|_{t=0}^{t=t_{\mathrm{end}}} \\
& + \oint\limits_{(\partial \Omega_{0,s} \times T)} \frac{\partial j_\Gamma}{\partial d_i} \left(\delta d_i\right) - \widehat{d}_i \left(\mathrm{D}_{iJkL} \, \frac{\partial \left(\delta d_i\right)}{\partial X_I} \right) d\Gamma_J^\tau \\
& - \int\limits_{\Gamma_{\mathrm{IF}}} \left(\delta d_i\right) \widehat{\kappa}_i \; d\Gamma \Bigg|_{t=0}^{t=t_{\mathrm{end}}} + \int\limits_{(\Gamma_{\mathrm{IF}} \times T)} \left(\delta d_i\right) \frac{\partial \widehat{\kappa}_i}{\partial t} \; d\Gamma^\tau \\
\stackrel{!}{=} \; & 0 \qquad \forall \, \delta d_i \in S_{\mathrm{ad}}
\end{aligned} \tag{26}
$$

Again, we require the integrands in eq. (26) to vanish and obtain in the next step by ignoring the contributions on the FSI-interface Γ_{IF} from the variation of structural displacements

$$
\int\limits_{(\Omega_{s,o} \times T)} \rho_s \left(\delta d_i\right) \frac{\partial^2 \widehat{d}_i}{\partial t^2} + \frac{\partial \widehat{d}_i}{\partial X_J} \, \mathrm{D}_{iJkL} \, \frac{\partial \left(\delta d_i\right)}{\partial X_I} + \frac{\partial j_{\Omega_s}}{\partial d_i} \left(\delta d_i\right) d\Omega_0^\tau = 0 \quad \forall \, \delta d_i \in S_{\mathrm{ad}}
$$

$$
\text{in } \left(\Omega_{s,o} \times T\right) \tag{27}
$$

$$
\widehat{d}_{i,(t=t_{end})} = 0 \quad \text{in} \quad \left(\Omega_{s,o}\right) \tag{28}
$$

$$
\frac{\partial \widehat{d}_i}{\partial t}_{\,(t=t_{end})} = 0 \quad \text{in} \quad \left(\Omega_{s,o}\right) \tag{29}
$$

$$
\widehat{d}_i = 0 \quad \text{on } \left(\Gamma_D \backslash \Gamma_{IF}\right) \tag{30}
$$

$$
\frac{\partial \widehat{d}_i}{\partial X_J} = 0 \quad \text{on } \left(\Gamma_N \backslash \Gamma_{IF}\right) \quad . \tag{31}
$$

The tangent stiffness tensor $\mathrm{D}_{iJkL} = \mathrm{F}_{iI} \mathbb{C}_{IJKL} \mathrm{F}_{kK} + \delta_{ik} \mathbb{S}_{JL}$ is a function of the structural deformation d_i with deformation gradient F_{kK}, elasticity tensor $\mathbb{C}_{IJKL}$ and second Piola-Kirchhoff stress tensor $\mathbb{S}_{JL}$. Since the Lagrange multiplier $\widehat{d}_i$, described by eq. (27) in a weak sense, shows an analogous behaviour to the primal structural displacement d_i described by eq. (3), it is also called "adjoint structural displacement" and from here onwards, eq. (27) is referred to as "adjoint structure equation" in its weak form. The latter equations (28) - (31) define necessary boundary conditions to solve the adjoint structure problem (27). The boundary sections Γ_D and Γ_N denote the Dirichlet and Neumann boundary respectively of the structural domain $\Omega_{s,o}$ in its reference configuration.

At this stage, we have not discussed so far how to treat the contributions over the FSI-interface in eq. (19) and (26). The requirement of a vanishing total derivative $\delta\mathcal{L} = 0$ can at this stage be achieved by requiring

$$\int\limits_{(\Gamma_{\text{IF}}\times T)} \left(\delta v_i\right) \widehat{\kappa}_i + \left(\delta d_i\right) \frac{\partial \widehat{\kappa}_i}{\partial t}\; d\Gamma^\tau - \int\limits_{\Gamma_{\text{IF}}} \left(\delta d_i\right) \widehat{\kappa}_i\; d\Gamma \Bigg|_{t=0}^{t=t_{\text{end}}} \stackrel{!}{=} 0 \quad \forall\, \delta y \in Y_{\text{ad}}\,. \tag{32}$$

From the FSI-framework, we recall the equality of test functions $\delta v_i = \delta d_i$ on the FSI-interface Γ_{IF} and by introducing superindices $(\cdot)^f$ and $(\cdot)^s$ for contributions of fluid and structure respectively, we obtain

$$\int\limits_{(\Gamma_{\text{IF}}\times T)} \left(\delta d_i\right) \left\{ \widehat{\kappa_i}^f + \frac{\partial \widehat{\kappa_i}^s}{\partial t} \right\} d\Gamma^\tau - \int\limits_{\Gamma_{\text{IF}}} \left(\delta d_i\right) \widehat{\kappa_i}^s\; d\Gamma \Bigg|_{t=0}^{t=t_{\text{end}}} \stackrel{!}{=} 0 \quad \forall\, \delta y \in Y_{\text{ad}}\,. \tag{33}$$

From a fluids point of view, we can interpret the Lagrange multiplier $\widehat{\kappa_i}^f$ on the FSI-interface Γ_{IF} as a test function of the associated coupling variable, which allows us to identify $\widehat{\kappa_i}^f$ on the FSI-interface with the adjoint velocity $\widehat{v}_i$. Keeping in mind the different direction of integration over the coupling boundary Γ_{IF} from a structural point of view, we obtain analogously $\widehat{\kappa_i}^s = -\widehat{d}_i$ on the FSI-interface. Therefore, the first component in eq. (33) vanishes for

$$\widehat{v}_i \;=\; \dot{\widehat{d}}_i \quad \text{on} \quad (\Gamma_{\text{IF}}) \tag{34}$$

which yields as in eq. (4) an "adjoint FSI-coupling condition" for the FSI-interface Γ_{IF}. From the second term in eq. (33) we conclude then by application of eq. (34) $\widehat{v}_i(t = t_{\text{End}}) = \dot{\widehat{d}}_i(t = t_{\text{End}}) = 0$.

Recapitulating the adjoint equations obtained from the optimality conditions from subsection 2.2, we can now formulate the complete adjoint FSI-problem by

$$\begin{aligned}
-\frac{\partial \widehat{v}_i}{\partial t} - \left(v - v_m\right)_j \frac{\partial \widehat{v}_i}{\partial x_j} - v_j \frac{\partial \widehat{v}_j}{\partial x_i} + \frac{\partial}{\partial x_j}\left[\widehat{p}\,\delta_{ij} - 2\nu\,\widehat{S}_{ij}\right] &= -\frac{\partial j_{\Omega_f}}{\partial v_i} && \text{in} \quad \Omega_f^\tau \\
\frac{\partial \widehat{v}_i}{\partial x_i} &= \frac{\partial j_{\Omega_f}}{\partial p} && \text{in} \quad \Omega_f^\tau \\
\int\limits_{(\Omega_o^s\times T)} \rho_s\left(\delta d_i\right) \frac{\partial^2 \widehat{d}_i}{\partial t^2} + \frac{\partial \widehat{d}_i}{\partial X_J}\,\mathrm{D}_{iJkL}\,\frac{\partial\left(\delta d_i\right)}{\partial X_I} + \frac{\partial j_{\Omega_s}}{\partial d_i}\left(\delta d_i\right)\, d\Omega_0^\tau &= 0 && \text{in} \quad \Omega_{s,o}^\tau \\
\widehat{v}_i \;&=\; \dot{\widehat{d}}_i && \text{on} \quad \Gamma_{\text{IF}}^\tau.
\end{aligned} \tag{35}$$

To provide suitable FSI-coupling for the adjoint FSI-problem above, we require in addition to the adjoint coupling condition (34) an equilibrium of the adjoint tractions at the fluid-structure interface $\Gamma_{\mathrm{IF}}^{\tau}$ as proposed by [11]. As in the case of the primal FSI-problem (8), we are faced in the adjoint case with a continuous formulation of both structural and fluid domain connected by a shared interface requiring an equality of the adjoint test functions at the coupling interface $\Gamma_{\mathrm{IF}}^{\tau}$.

2.4 Numerical properties of the adjoint problem

As the primal FSI-problem (8), the derived adjoint FSI-problem (35) has to be solved at a numerical level and since its structure is very similar to the primal FSI-problem (8), we recommend to access solution structures from the primal solution process as far as possible. Nonetheless, there are some major differences in the behaviour of primal and adjoint equations which shall be briefly discussed in this subsection.

Recapitulating the adjoint momentum equation (20), we face a different behaviour in time in the adjoint system. A change of the direction in time is characteristic of adjoint systems of time-dependent problems and since we have to compute the adjoint solution backwards in time, we obtain in eq. (21), (28) and (29) boundary conditions at the end of the simulation time t_{end}. Hence, the first step consists in calculating the solution of the primal FSI-problem (8) from starting time t_0 to end time t_{end}, since information about the primal state is required in terms of the adjoint solution process. The adjoint system is then advanced backwards in time from t_{end} to t_0 in a second step by referring to required primal information. In this context, the use of proper temporal differencing schemes must be provided during the adjoint solution process.

The same effect can be observed in the behaviour of the adjoint convection term in eq. (20). As a consequence of integration by parts, there is a shift in the sign of the adjoint convection term $(v - v_m)_j \frac{\partial \widehat{v}_i}{\partial x_j}$. Since convection is an effect directed in space, upwind discretization schemes are usually applied during the primal solution process to ensure proper capturing of convection effects. The shift in the sign of the adjoint convection demands in this case the application of downwind differencing schemes during the adjoint solution process.

Both primal and adjoint FSI-problem are solved in a partitioned framework taking advantage of the finite volume method solving the flow field and of a finite element approach solving the structural problem respectively [15]. The solution in the fluid domain Ω_f^{τ} is realized by usage of the finite volume solver library OpenFOAM® [16] which allows the implementation of appropriate variations of the PISO-algorithm [17]. Since the arteries are modelled as thin-walled hyperelastic marterials, we apply a high-order finite element formulation during the structural solution process being less prone to locking effects and mesh distortion [18][19].

The partitioned coupling between fluid and structural mechanics problem during primal and adjoint solution process is realized by the use of a coupling interface [20][21] based on a quasi-Newton acceleration procedure. The solution of the FSI-problems (8) and (35) is then performed in an iterative manner by an exchange of information between displacement and flow field provided by the employed coupling interface.

3 Gradient computations

After the derivation of the adjoint FSI-problem in eq. (35), subsection 3.1 discusses how to compute a feasible surface sensitivity by exploitation of the remaining optimality condition. As illustrated in Figure 1, knowledge of this surface sensitivity allows then to compute the gradient of the considered cost functional by solving an additional PDE as shown in subsection 3.2.

3.1 Computation of a proper surface sensitivity

At this stage, we assume the solution of the adjoint FSI-problem (35) to be already known and the derivatives $\delta_{\overline{p}}\mathcal{L}$, $\delta_v\mathcal{L}$ and $\delta_d\mathcal{L}$ of the Lagrange functional $\mathcal{L}$ vanish by construction of the adjoint system. Considering an optimal state, the total derivative of both cost and Lagrange functional will vanish. But since the shape to be optimized is more or less far away from this desired optimal state, the derivative $\delta_u\mathcal{L}$ will not vanish and defines therefore a deviation from the optimal state. The deviation from the latter optimality condition (14) $\delta_u\mathcal{L}\cdot\delta u = 0$ can now be used to derive a concrete description of a surface sensitivity $K(u)$ of the form $\int_\Gamma K(u)\cdot\delta u\ d\Gamma$.

Taking into account the primal FSI-problem (8) in its residual form, a first important remark can be made by considering the variation of the primal state equations. For the momentum equation R_i (1) holds for example

$$\begin{aligned} \delta\mathrm{R}_i \ &= \delta_{\overline{p}}\mathrm{R}_i + \delta_v\mathrm{R}_i + \delta_d\mathrm{R}_i + \delta_u\mathrm{R}_i = 0 \\ \Rightarrow \quad \delta_u\mathrm{R}_i &= -\big(\delta_{\overline{p}}\mathrm{R}_i + \delta_v\mathrm{R}_i + \delta_d\mathrm{R}_i\big) \quad . \end{aligned} \tag{36}$$

Equation (36) allows to express the derivative $\delta_u\mathrm{R}_i$ in terms of the already calculated derivatives $\delta_{\overline{p}}\mathrm{R}_i$, $\delta_v\mathrm{R}_i$ and $\delta_d\mathrm{R}_i$, which is analogously also possible for the derivatives of the continuity equation (2) and the structural mechanics equation (3) (see also [7][8]). Using eq. (36) as well as the results of subsection 2.3, and taking advantage of the approach proposed by [8]

$$\delta v_i \approx \frac{\partial v_i}{\partial u}\,\delta u \tag{37}$$

$$\delta p \approx \frac{\partial p}{\partial u}\,\delta u \tag{38}$$

$$\delta d_i \approx \frac{\partial d_i}{\partial u}\,\delta u \quad , \tag{39}$$

we obtain for the derivative of the Lagrange functional $\delta_u \mathcal{L}$ with respect to the control parameter u under consideration of the remaining terms defined over the fluid-structure interface $\Gamma_{\mathrm{IF}}^{\tau}$

$$\begin{aligned}\delta_u \mathcal{L} \cdot \delta u = \delta_u J \cdot \delta u \;\; &- \int\limits_{(\Gamma_{\mathrm{IF}} \times T)} \left\{ \left(v_j \widehat{v}_j - \widehat{p}\,\right) \frac{\partial v_i}{\partial u}\, n_i + \nu \frac{\partial v_i}{\partial u} \frac{\partial \widehat{v}_i}{\partial x_j}\, n_j - \nu\, \widehat{v}_j\, \frac{\partial (\frac{\partial v_i}{\partial u})}{\partial x_i}\, n_i \right\} \delta u \; d\Gamma^{\tau} \\ &- \int\limits_{(\Gamma_{\mathrm{IF}} \times T)} \frac{\partial d_i}{\partial u}\, \frac{\partial \{ \mathrm{D}_{iJkL}\, \widehat{d}_i \}}{\partial X_I}\, \delta u \; d\Gamma_J^{\tau} \quad . \end{aligned} \tag{40}$$

By construction of the Lagrange functional $\mathcal{L}$, the derivative of the Lagrange functional $\delta_u \mathcal{L}$ listed above is equivalent to the substantial derivative of the cost functional J. Therefore, eq. (40) represents a continuous formulation of a surface sensitivity required in the pursued optimization process described in Fig. 1.

3.2 Gradient calculus based on the Laplace-Beltrami operator

In our case, the control parameter u is the shape of the structure and correlates therefore with the domain boundary Γ. In this context, we require that the shape Γ can be parametrized by $H^1(\Gamma, \mathbb{R}^3)$-mappings, so that Γ admits the formulation of a feasible surface area. As in eq. (7), $H^1(\Gamma, \mathbb{R}^3)$ denotes the corresponding Sobolev space $W^{1,2}(\Gamma, \mathbb{R}^3)$. Furthermore, we require the deformations of the shape δu to be elements of $H^1(\Gamma, \mathbb{R}^3)$ allowing for a subsequent parametrization of the varied shape $\Gamma' = (\Gamma + \epsilon \cdot \delta u)$ by H^1-mappings. Since the state variable $y := y(u)$ is a function of the control parameter u, the introduced cost functional $J(y(u), u)$ can be reformulated as an equivalent cost functional $\widehat{J} := \widehat{J}(u)$ being just a functional of the control parameter u. Therefore, we now consider the derative $\widehat{J}'(u) = \delta_u \mathcal{L}(y(u), u)$ in eq. (40) as a functional just of the control parameter u

$$\widehat{J}'(u) : \qquad H^1(\Gamma, \mathbb{R}^3) \longrightarrow \mathbb{R} \quad . \tag{41}$$

Since the derivative $\widehat{J}'(u)$ is a linear and also bounded functional if $y(u)$ is sufficiently smooth, it is an element of $H^1(\Gamma, \mathbb{R}^3)^*$ denoting the dual space of $H^1(\Gamma, \mathbb{R}^3)$. Hence, we conclude from the Riesz representation theorem

$$\begin{aligned}\delta\widehat{J}(u,\delta u) = \left\langle \widehat{J}'(u),\delta u\right\rangle_{H^1(\Gamma,\mathbb{R}^3)^*,H^1(\Gamma,\mathbb{R}^3)} &= \left(\mathbf{R}\widehat{J}'(u),\delta u\right)_{H^1(\Gamma,\mathbb{R}^3)} \\ &= \left(\widehat{G}(u),\delta u\right)_{H^1(\Gamma,\mathbb{R}^3)} \quad \forall\,\delta u \in H^1(\Gamma,\mathbb{R}^3)\end{aligned} \tag{42}$$

where we identify the required gradient $\widehat{G}(u)$ of the cost functional $\widehat{J}(u)$ with the Riesz representative $\mathbf{R}\widehat{J}'(u)$ of the derivative $\widehat{J}'(u)$. In eq. (42), $\left(\widehat{G}(u),\delta u\right)_{H^1(\Gamma,\mathbb{R}^3)}$ denotes the scalar product of $\widehat{G}(u)$ and δu in $H^1(\Gamma,\mathbb{R}^3)$. The left hand side of eq. (42) can be computed by knowledge of primal and adjoint solutions via

$$\delta\widehat{J}(u,\delta u) = \left\langle \widehat{J}'(u),\delta u\right\rangle_{H^1(\Gamma,\mathbb{R}^3)^*,H^1(\Gamma,\mathbb{R}^3)} = \widehat{J}'(u)\cdot\delta u = \int_\Gamma K(u)\cdot\delta u\; d\Gamma \tag{43}$$

as shown in the previous subsection. Application of integration by parts to the scalar product at the right hand side of eq. (42) leads to the weak form of a partial differential equation for the gradient $\widehat{G}(u)$ defined over the manifold Γ.

$$\begin{aligned}\left(\widehat{G}(u),\delta u\right)_{H^1(\Gamma,\mathbb{R}^3)} &= \int_\Gamma \widehat{G}(u)\cdot\delta u + \nabla_\Gamma\widehat{G}(u)\cdot\nabla_\Gamma(\delta u)\; d\Gamma \\ &= \int_\Gamma \left[\widehat{G}(u) - \triangle_\Gamma\widehat{G}(u)\right]\delta u\; d\Gamma \qquad \forall\,\delta u \in H^1(\Gamma,\mathbb{R}^3)\end{aligned} \tag{44}$$

Hence, we obtain the required gradient by solving the additional PDE (45) defined over the boundary Γ making use of the Laplace-Beltrami operator $\triangle_\Gamma$ and of the surface sensitivity $K(u)$

$$-\triangle_\Gamma\widehat{G}(u) + \widehat{G}(u) = K(u) \quad . \tag{45}$$

At this stage, the question arises of how to compute values of the surface sensitivity $K(u)$, since the surface sensitivity obtained in eq. (40) is still formulated in terms of the variation of the control parameter δu. Keeping in mind, that δu is an element of $H^1(\Gamma,\mathbb{R}^3)$, we have now to discuss the meaning of δu in the context of a discrete formulation. Since we are not able to maintain the continuous formulation of eq. (40) on a numerical level, we have to find a formulation of the shape deformation δu being useful in terms of a numerical implementation.

Keeping in mind, that the deformations δu represent small variations of the shape, we assume the deformations to be directed almost normal to the

surface of the shape. Motivated by this, we make the following assumption also used by [7] and [8] to find a discrete approximation of the surface sensitivity $K(u)$ definded in eq. (40)

$$\frac{\partial v_i}{\partial u}\,\delta u \approx \frac{\partial v_i}{\partial x_n}\,\delta n, \quad \frac{\partial p}{\partial u}\,\delta u \approx \frac{\partial p}{\partial x_n}\,\delta n, \quad \frac{\partial d_i}{\partial u}\,\delta u \approx \frac{\partial d_i}{\partial x_n}\,\delta n \quad . \tag{46}$$

The shape variation δu and its associated derivates are approximated in eq. (46) by the product of derivatives $\partial/\partial x_n$ in the direction of the local normal vector n_i of the related boundary Γ with its corresponding variation δn.

In fact, the approach introduced in eq. (46) is not feasible from a continuous point of view since it is based on deformations defined in terms of $\mathbb{R}^3$ resulting in varied shapes not being part of $H^1(\Gamma, \mathbb{R}^3)$ anymore. But since the approach (46) is used on a numerical level only, deformations according to eq. (46) relate only to deformations of the discrete nodes of the surface. These variations lead to a deformation of the whole surface constituting a $H^1(\Gamma, \mathbb{R}^3)$-surface from the the varied surface nodes whose deformations are close to the normal direction being therefore approximated discretely via eq. (46).

Knowledge of the normal vector and derivatives in the normal direction on a numerical level allows therefore the computation of the surface sensitivity by reformulating eq. (40) using the discrete approach introduced in eq. (46).

$$\begin{aligned}\delta_u\mathcal{L}\cdot\delta u = \delta_u J\cdot\delta u \;\; &- \int_{(\Gamma_{\mathrm{IF}}\times T)} \left\{ \left(v_j\widehat{v}_j - \widehat{p}\,\right)\frac{\partial v_n}{\partial x_n} + \nu\frac{\partial v_i}{\partial x_n}\frac{\partial \widehat{v}_i}{\partial x_n} - \nu\,\widehat{v}_j\,\frac{\partial^2 v_j}{\partial x_n^2}\right\}\delta n\;\, d\Gamma^\tau \\ &- \int_{(\Gamma_{\mathrm{IF}}\times T)} \frac{\partial d_i}{\partial X_N}\,\frac{\partial\{\mathrm{D}_{iJkL}\,\widehat{d}_i\}}{\partial X_N}\,\delta n\;\, d\Gamma_0^\tau \end{aligned} \tag{47}$$

In this work, we focus on cost functionals being just defined over inlet and outlet parts of the flow domain and since inlet and outlet parts are not affected by the optimization process, the local variation of the cost functional represented by the term $\delta_u J\cdot\delta u$ vanishes. By construction of the Lagrange functional, $\delta_u\mathcal{L}$ is equivalent to the substantial derivative of the cost functional J and the integral components of eq. (47) match with the convective variation of the cost functional J with respect to the control parameter u. In the context of the pursued optimization process described in Figure 1, the surface sensitivity $K(u)$ defined by eq. (47) as

$$K(u) \;=\; \left(\widehat{p} - v_j\widehat{v}_j\,\right)\frac{\partial v_n}{\partial x_n} - \nu\frac{\partial v_i}{\partial x_n}\frac{\partial \widehat{v}_i}{\partial x_n} + \nu\,\widehat{v}_j\,\frac{\partial^2 v_j}{\partial x_n^2} - \frac{\partial d_i}{\partial X_N}\,\frac{\partial\{\mathrm{D}_{iJkL}\,\widehat{d}_i\}}{\partial X_N} \tag{48}$$

can then be used as a template to compute the gradient $\widehat{G}(u)$ required in the framework of a steepest descent algorithm by solving the Laplace-Beltrami-PDE (45) as explained above.

4 Application to multidimensional ducted flows

According to Figure 1, the gradient calculated by solving the PDE (45) can now be used in the context of a steepest descent algorithm to improve shapes of overflowed structures. In the following section, we show the performance of the adjoint-based optimization strategy by an application to ducted flows. The first example in subsection 4.1 shows the deformation of an overflowed 2D-cylinder and allows, due to its rather academical character, a brief evaluation of the optimization behaviour. In subsection 4.2, the control strategy is applied to an artificial artery to demonstrate the functionality of the realized optimization process in complex engineering applications.

In both examples, the dissipation of energy due to the resulting pressure drop in the fluid is supposed to be minimized by small variations of the structural shape. Since in a ducted flow the pressure drop is calculated by the differences of static and dynamic pressure between inlet and outlet, there is no contribution of the cost functional inside the physical domain and we hold $j_\Omega = 0$ for the considered cost functional. Hence, the cost functional J associated with the dissipation of energy caused by the fluid's pressure drop can be formulated as

$$J \;:=\; J_\Gamma = -\int_{t_0}^{t_{\text{end}}} \int_{\Gamma_f} \left(p + \rho_f \, \frac{v_j \, v_j}{2} \right) v_i \, n_i \;\, d\Gamma \, dt \quad . \tag{49}$$

Therefore, all derivatives concerning contributions of the cost functional inside the physical domain vanish and for the respective components in the adjoint FSI-problem (35) holds

$$\frac{\partial j_{\Omega_f}}{\partial v_i} = \frac{\partial j_{\Omega_f}}{\partial p} = \frac{\partial j_{\Omega_s}}{\partial d_i} = 0 \quad . \tag{50}$$

Furthermore, the above formulated cost functional allows to determine the contributions of the cost functional to the boundary conditions (18), (24) and (25) by computing the required derivatives on the boundary.

$$\frac{\partial j_{\Gamma_f}}{\partial p} = -v_i \, n_i \qquad\qquad \frac{\partial j_{\Gamma_f}}{\partial v_i} = -\left(p + \rho_f \, \frac{v_j v_j}{2} \right) n_i - \left(v_k \, n_k \right) v_i \tag{51}$$

Minimization of pressure drop and its associated drag force by modification of the shape is a common fluid dynamic design task and is therefore chosen in this work to demonstrate potential and practical value of the developed optimization strategy in demanding engineering applications.

4.1 Deformation of a two-dimensional cylinder section

The first example shows the laminar flow over a two-dimensional cylinder section which is located in the center of the flow channel and whose structure deforms due to fluid loads. The case setup is shown in Figure 3 including both geometry and physical boundary conditions in the channel. The inlet velocity of the fluid is oscillating with a frequency of 10 [Hz] around an averaged value of $\overline{v}_{\text{In}} = 0.2\ {}^{m}/s$ which causes periodic loads on the cylindric structure. The characteristic height of the flow channel is $H = 0.002$ [m] and the kinematic viscosity of the fluid is assumed as $\nu = 10^{-6}$ [m^2/s] from which the Reynolds number Re can be computed as

$$Re_{2D} = \frac{\overline{v} \cdot H}{\nu} = \frac{0.2\,[\text{m/s}]\ \cdot 0.002\,[\text{m}]}{10^{-6}\,[\text{m}^2/\text{s}]} = 400 \quad . \tag{52}$$

For the structure of the modelled FSI-cylinder section in the middle of the channel a constant Young's modulus of $E = 5 \cdot 10^4\,[\text{N/m}^2]$ is chosen to achieve large deformations during the simulation. The overall simulation period is $t_{\text{End}} = 1$ [s] and is once computed forward to solve the primal FSI-problem (8) and then advanced backwards during the adjoint solution process. In both cases, a constant time step size of $\triangle t = 0.001$ [s] is chosen.

The discretization of both flow channel and structure is shown in Figure 4 and allows a quick overview over the applied mesh setup. Taking into account the more complex flow situation in the cylinder region, the flow domain Ω_f is discretized by $80 \times 25 \times 1 = 2000$ cells taking advantage of a mesh refinement towards the middle of the channel. The second view of Figure 4 allows a more detailed view of the structural mesh and of the associated FSI-interface between fluid and structural mesh. The structural domain Ω_s is discretized by $50 \times 3 \times 1 = 150$ cells leading to similar mesh resolutions for fluid and structure in the interface region.

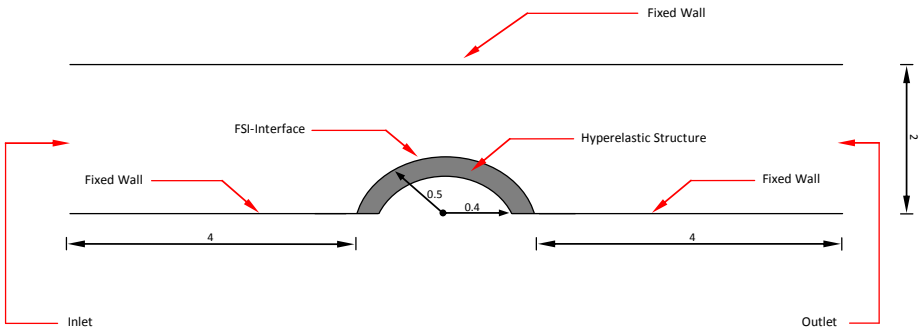

Abb. 3 Geometry and physical boundary conditions in the considered 2D flow channel.

Figure 5 shows the primal velocity field at the end of the simulation at $t_{\text{End}} = 1$ [s] and the adjoint flow field at $t_0 = 0$ [s] respectively. The snapshot of the primal fluid velocity field (top of Figure 5) shows the deformation of the cylindric structure at the end of the simulation and an acceleration of the flow at the end of the channel due to the separation behind the cylinder. The adjoint velocity field beneath at $t = t_0$ illustrates the shift in the convective behaviour of the adjoint Navier-Stokes equations.

Since a reduction of the pressure drop in the fluid is realized just by variation of the shape of the FSI-interface, we compute according to Figure 1 in a subsequent step the distributions of surface sensitivity $K(u)$ and gradient $\widehat{G}$ of the cost functional J over the cylindric structure in the channel. In Figure 6, both sensitivity and gradient field are displayed by proper scaling of the associated normal vector $\mathbf{n}$.

Figure 6 illustrates the difference between surface sensitivity and gradient in the context of a steepest descent algorithm. In this example, it is from a technical point of view obvious, that a reduction of the fluid's pressure drop demands a homogeneous decrease of the cylinder inside the flow region of the channel since from a fluids point of view the optimal geometry would be a flat, viscous wall. Although the calculated sensitivity field (left of Figure 6) suggests a deformation reducing the bulge inside of the flow field, an exceeding preference of the structure in the fore of the cylinder can be observed. Following a deformation according to the sensitivity in Figure 6, rear regions of the cylinder would not be deformed at all.

In contrast to this, the computed gradient leads to the expected optimization instruction as shown in Figure 6 on the right. Furthermore, the computed gradient field shows, due to the structure of eq. (45), a significant smoother behaviour meaning a substantial advantage during the subsequent mesh mor-

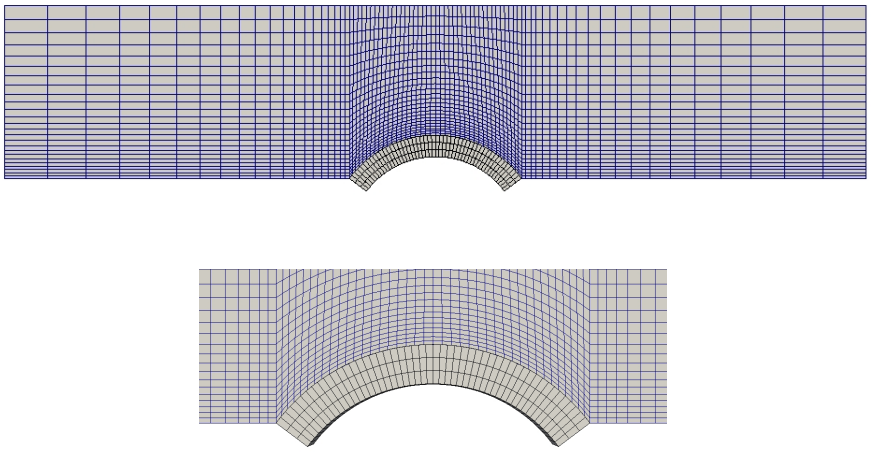

Abb. 4 Discretization of flow channel (blue) and structure (black). View of the complete mesh model (top) and the FSI-interface in detail (bottom).

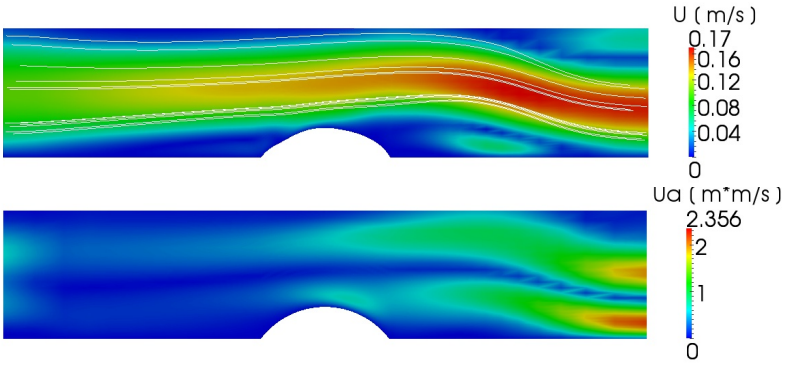

Abb. 5 Primal velocity field at $t_{\mathrm{End}} = 1$ [s] (top) and adjoint velocity field at $t_0 = 0$ [s] (bottom) in consideration of interactions between fluid and structure.

phing performed in the framework of the optimization strategy proposed in Figure 1. In conjunction with its normal vector field, the gradient field on the right of Figure 6 defines the desired instruction of how to change the shape of the cylindric structure to reduce the pressure drop in the flow field. A graphic analysis of the distribution of the suggested shape modifications, as presented in Figure 7, shows in addition to Figure 6 range and dimension of the computed morphing instruction for the structure of the cylinder.

In the next step, the shape of the cylinder is modified according to the gradient distribution of Figure 6 and the whole optimization process consisting of solving primal FSI-system (8), adjoint FSI-system (35), surface sensitivity (47) and gradient equation (45) with subsequent mesh morphing is repeated in an iterative manner. In this context, Figure 8 shows the shape of the involved structure before and after the first optimization loop. As demanded from the gradient distribution in Figure 6, a continuous decrease of the shape curvature inside the flow channel is achieved during the mesh morphing process.

In this example, the optimization loop is performed for five times with an overrelaxated gradient stepsize α by a factor of five in favour of an acceleration

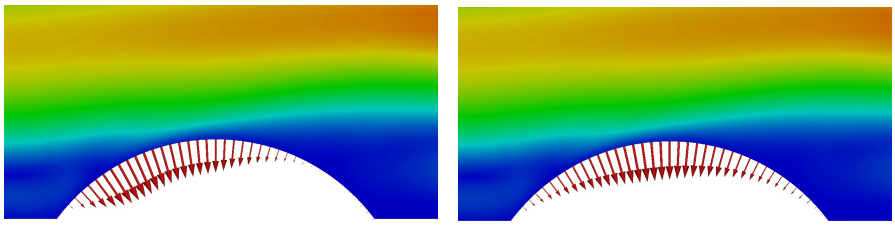

Surface sensitivity field Surface Gradient field

Abb. 6 Sensitivity vs. gradient of the cost functional J on the FSI-interface illustrated by scaling of the associated normal vector $\mathbf{n}$.

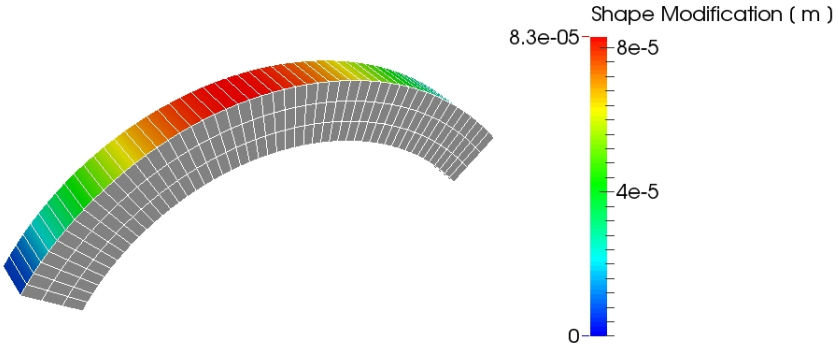

Abb. 7 Shape modification of the structure gained in the course of the first optimization loop.

of the improvement during one optimization step. This can be motivated by a comparison of the results using different gradient stepsizes α as shown in Figure 9. The blue line in Figure 9 shows the reduction of dissipated work in the fluid after one optimization loop using a non-relaxated gradient step as in the usual steepest descent algorithm meaning a stepsize of $\alpha = 1$. Analogously, the green line represents the reduction of the dissipated work in the fluid after one optimization loop employing an overrelaxated gradient stepsize of $\alpha = 20$ in the performed mesh morphing. The red line in Figure 9 shows the reduction of the dissipated work after every single optimization loop using an overrelaxated gradient stepsize of $\alpha = 5$. Therefore, the first data point of the red line marks the reduction of dissipated work after the first optimization loop using a stepsize of $\alpha = 5$.

For the overflowed cylinder, Figure 9 shows on the one hand, that the best result after one optimization loop is obtained by using a highly overrelaxated gradient stepsize (e.g. $\alpha = 20$). On the other hand, Figure 9 shows, that the quality of the results increases by using smaller gradient steps and more optimization loops which is not surprising in the context of a steepest descent algorithm. Since the initial slope of the red line is almost equivalent to the slope of the non-overrelaxated gradient step (blue), a stepsize of $\alpha = 5$ seems to be a

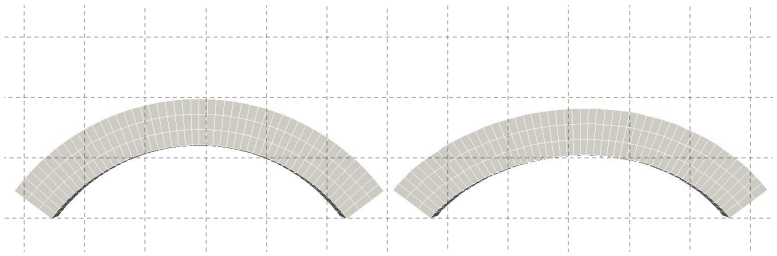

Abb. 8 Initial shape (left) vs. optimized shape (right) of the cylinder structure after the first optimization loop and an gradient stepsize of $\alpha = 5$.

very good compromise between saving numerical effort and the superior quality of small gradient steps. A detailed study about optimal gradient stepsizes in the context of adjoint-based optimization techniques can be found in [25], where the application of proper formulations of the Armijo algorithm in the context of a steepest descent algorithm is discussed. After having passed five optimization loops with a stepsize of $\alpha = 5$, the obtained cylinder geometry achieves a reduction in the dissipated work caused by the fluids pressure drop of 8.53 %.

Summarizing the results of this example, we observe, on the one hand, a feasible behaviour of the computed gradient $\widehat{G}$ in terms of a steepest descent framework. On the other hand, application of the proposed optimization strategy leads to a serious improvement of the considered cost functional in this rather academical case. In the next subsection, we extend the presented optimization method to the design of artificial arteries to show the functionality of the realized algorithm in complex shape design problems.

4.2 Dissipated energy in an artificial blood vessel

In this section, the developed optimization algorithm is expanded to three-dimensional flows to evaluate the optimization behaviour in more demanding flow situations. In this case, we consider an S-shaped model artery whose walls deform due to the periodic fluid loads in the human cardiovascular system. Figure 10 illustrates the geometric dimensions and the boundary conditions inside the flow channel. Again, we consider a laminar flow with a Reynolds number of

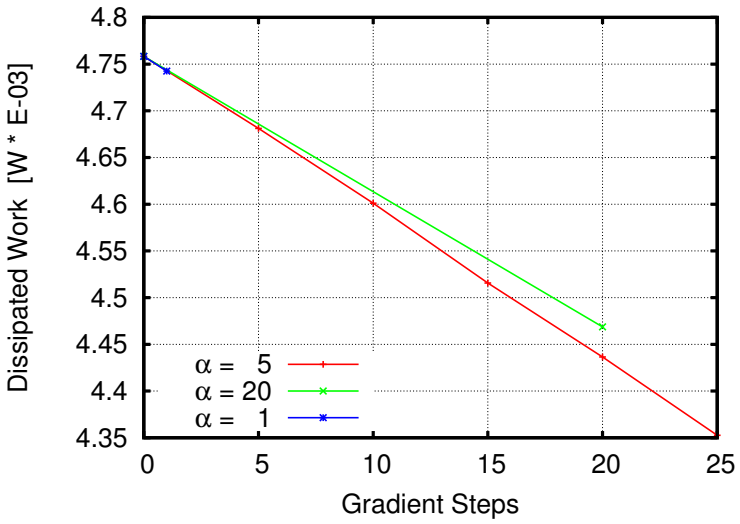

Abb. 9 Differences in the gained reduction of dissipated work due to application of different gradient stepsizes.

$$Re_{3D} = \frac{\overline{v} \cdot D}{\nu} = \frac{0.2\,[\mathrm{m/s}]\ \cdot 0.01\,[\mathrm{m}]}{10^{-5}\,[\mathrm{m^2/s}]} = 200 \tag{53}$$

with velocities oscillating with a frequency of 10 [Hz] around a reference velocity of $\overline{v} = 0.2$ [m/s]. In addition to the oscillating velocity profile at the inlet, the pressure at the outlet of the artery is oscillating with the same frequency around a reference pressure of $p_{\mathrm{ref}} = 12500$ [Pa] to simulate the pulsating flow conditions of the human cardiovascular system.

Motivated by [22] and [23], blood is treated in this work for the sake of simplificity as a Newtonian fluid with a kinematic viscosity of $\nu = 10^{-6}[\mathrm{m^2/s}]$. As shown in Figure 10, the characteristic diameter D of the considered artery is modeled with $D = 10$ [mm] representing characteristic dimensions of an artery in the human body. Due to the high fluctuations in the considered flow conditions, we expect large deformations in the structure of the model artery and assume the whole interior part of the structure as an interface affected by interactions between fluid and structure. In order to decrease the negative influence of mesh distortion and locking effects, shape functions up to a polynomial degree of $p_{\mathrm{FEM}} = 4$ are applied during the computations to improve the quality of both primal and adjoint structural mechanics problems. Again, a period of $t_{\mathrm{End}} = 1$ [s] is considered and computed forward in time using the Newmark time-integration method in terms of the primal solution process. The adjoint FSI-problem (35) is then calculated backwards in time from $t_{\mathrm{End}} = 1$ [s] to $t_0 = 0$ [s] by application of a proper Newmark time-integration method taking account of the shift in the direction of time.

The discretization of both vascular wall and flow channel inside of the model artery are shown in Figure 11. The fluid mesh (blue) is discretized by $500 \times 200 = 100,000$ cells using 500 cells in longitudinal direction and 200 cells in each longitudinal plane. In contrast to this, the structural mesh of the blood vessel is realized by much larger elements leading to a far coarser mesh consisting of $100 \times 20 \times 2 = 4,000$ hexahedral elements where 100 cells were used in longitudinal direction. The structure of the vascular wall in one longitudinal section is discretized by two cells in radial direction and 20 cells in angular direction respectively.

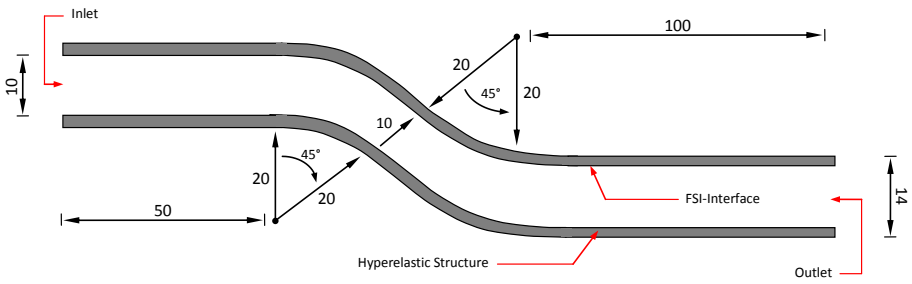

Abb. 10 Geometry and physical boundary conditions in the considered model artery.

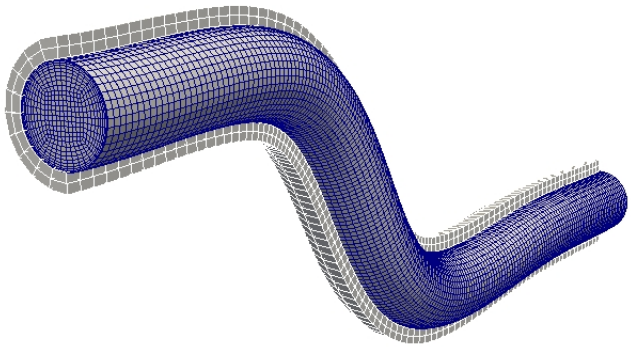

Abb. 11 Discretization of the vascular wall (grey) and the flow domain inside of the artery (blue).

The calculated flow fields are shown in Figure 12, where the primal velocity field at the end of the simulation $t_{\mathrm{End}} = 1$ [s] is presented above the adjoint flow field at $t_0 = 0$ [s]. In both cases the flow field is illustrated by a representative slice through the median longitudinal plane of the artery allowing an overview over the flow situation along the length of the vessel.

Considering the primal flow field in Figure 12, it can be observed in the entrance and exit regions of the S-bend that the fluid flow is again not able to follow the shape of the considered artery completely leading to a separation in the flow field behind the first bending section. Due to this separation, the fluid is accelerated in regions near the wall opposite to the inlet of the model artery. After having passed the second bend in the shape of the artery, the flow field is restructuring to the expected velocity profile at the outlet of the vessel. As seen in the two-dimensional example before, the adjoint velocity field in Figure 12 is dominated by the shift in the direction of the convective flow behaviour. The acceleration of the adjoint flow at the outlet of the artery is caused by the choice of the respective boundary conditions previously discussed in section 2.3.

As in the previous example, the next step consists in calculating the surface sensitivity according to eq. (47) and its associated gradient field. Figure 13 shows the distribution of the surface sensitivity over the inner wall of the artery. The first view above illustrates the differences in the magnitude of sensitivity values along the artery which is characteristic behaviour of surface sensitivities in ducted flows. In regions near both inlet and outlet, sensitivity values are overshooted by a factor of around 100 compared to the rest of the vascular wall. In order to show the behaviour of the computed sensitivity field over the main part of the vessel wall, Figure 13 shows a second view of the sensitivity purged of the peak values at inlet and outlet regions. This purged view of the computed sensitivity field points up a rough and inhomogeneous

behaviour of the surface sensitivity in terms of shifts in sign and magnitude being characteristic of sensitivity distributions as well.

In the context of the optimization strategy proposed in Figure 1, both aspects cause a decrease in quality and stability of the pursued optimization framework. So from both a technical and a theoretical point of view, it is obvious that a shape optimization according to surface sensitivities, as misleadingly performed in lots of engineering applications, leads to suboptimal variations in the shape.

Compared to this, the associated gradient field $\widehat{G}$, illustrated in Figure 14 by proper scaling of the normal vector field $\mathbf{n}$, shows significant favourable properties in terms of both smoothness and fluctuations in magnitude. As suggested in Figure 14, the calculated gradient field proposes a consequent expansion of the diameter over the main part of the considered model artery. From a technical point of view, the morphing prediction obtained by the gradient in Figure 14 represents a reasonable result since in a ducted flow an expansion of the encountered diameter usually results in a decrease of the fluids pressure drop.

In a subsequent step, the geometry of the considered model artery is deformed according to the gradient distribution presented in Figure 14 in terms of a steepest descent algorithm. The resulting modification of the initial shape

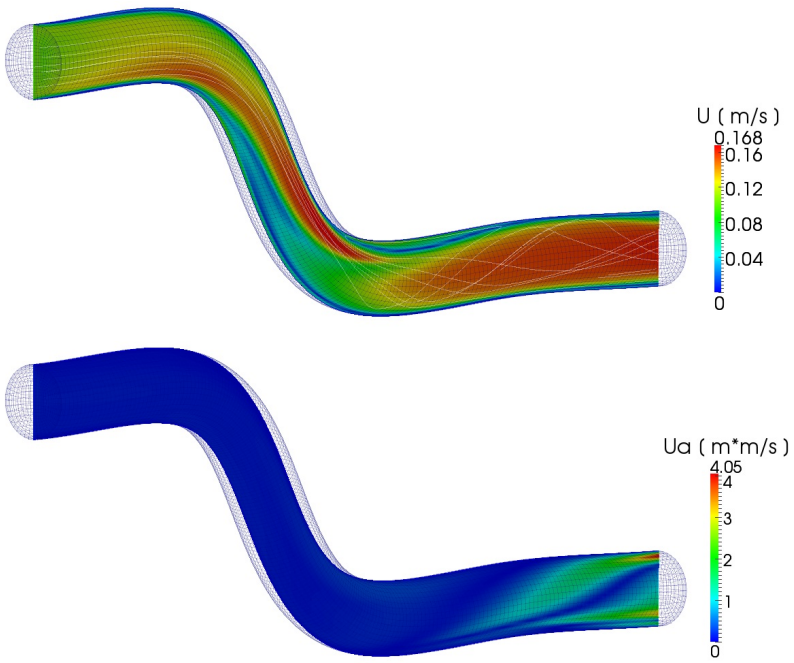

Abb. 12 Primal (top) and adjoint velocity field (bottom) in an artificial blood vessel in consideration of interactions between fluid and structure at $t_{\mathrm{End}} = 1$ [s] (top) and $t_0 = 0$ [s] (bottom) respectively.

of the blood vessel is illustrated in Figure 15 and shows the small dimensions of the changes in the shape of the concerned model artery.

Since we are faced in this example with a tremendous computational effort concerning time and memory, the stepsize of the performed steepest descent algorithm is again overrelaxated by a factor of five legitimated by the good experiences gained in section 4.1. The primal FSI-problem (8) is solved for the modified geometry and the whole optimization process is repeated iteratively twice. As seen before in Figure 9, Figure 16 shows the gain in performance due to the reduction of the fluids pressure drop in course of the single optimization steps. The green line shows the optimization by application of an overrelaxated gradient stepsize by a factor of $\alpha = 10$, whereas the red line represents the iterative optimization loops described above using a gradient stepsize of $\alpha = 5$. Again it can be observed, that the smaller stepsize leads to better results at the expense of computational time. After having passed the optimization loop three times, we observe a decrease of 15.13 % in the pressure drop of the blood flow.

Recapitulating the results discussed above as well as the results from section 4.1, we note a positive behaviour of the developed optimization method concerning efficiency, robustness and physical plausibility. Application of the

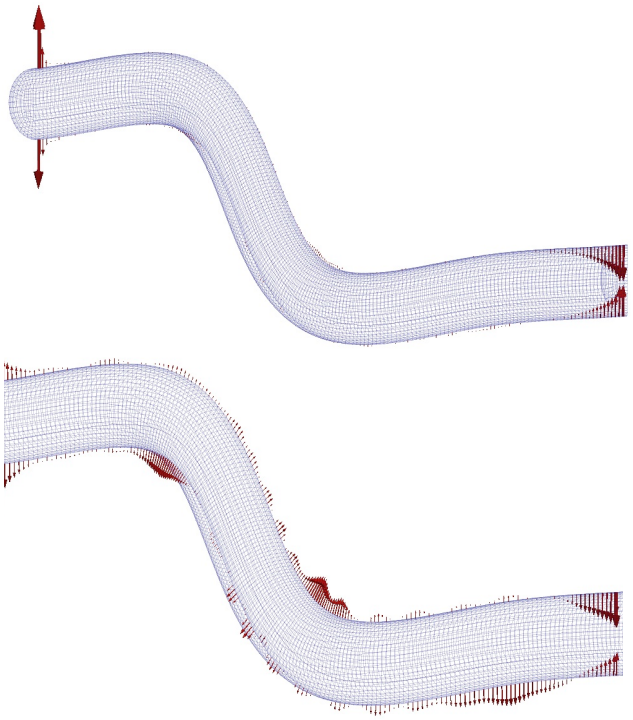

Abb. 13 Surface sensitivity field of the cost functional J over the inner wall of the artery illustrated by scaling of the associated normal vector $\mathbf{n}$.

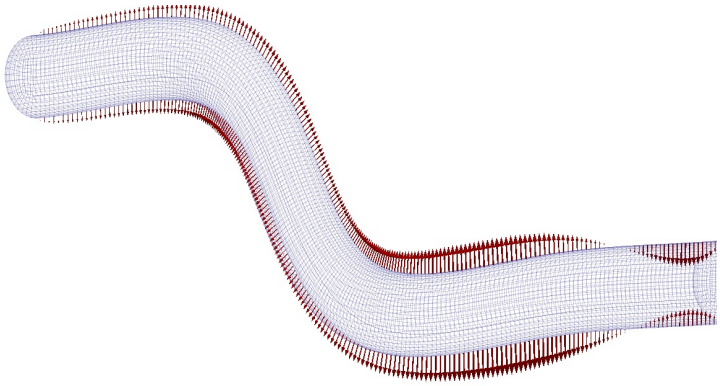

Abb. 14 Gradient field of the cost functional J over the inner wall of the artery illustrated by scaling of the associated normal vector $\mathbf{n}$.

optimization algorithm proposed by Figure 1 leads in both examples to a significant decrease in the pressure drop of the involved fluid flows. In both examples, the developed method is able to provide morphing instructions being appropriate in the context of an adjoint-based design process. The calculated gradient fields are distinguished by smooth distributions proposing meaningful deformations of the considered geometries which is required for a capable optimization framework in terms of computational efficiency and robustness.

5 Conclusions

According to the primal time-dependent FSI-problem, adjoint equations and coupling conditions are derived and solved in the framework of a fully coupled, partitioned solution approach. In this context, an adjoint fluid-solver adapted to the ALE-formulation in fluid mechanics is developed as well as an

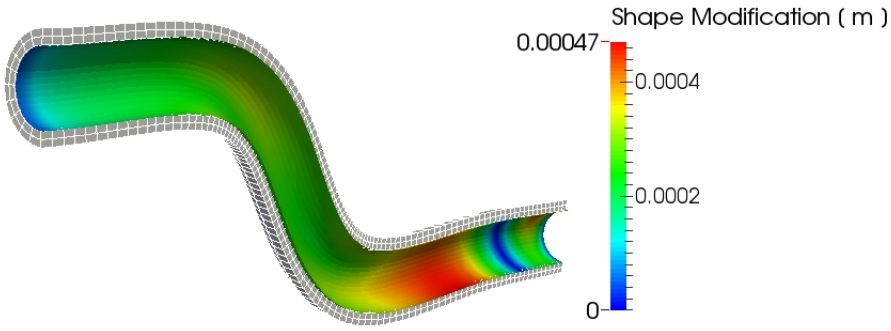

Abb. 15 Shape modification for the vascular wall according to the gradient distribution presented in Figure 14.

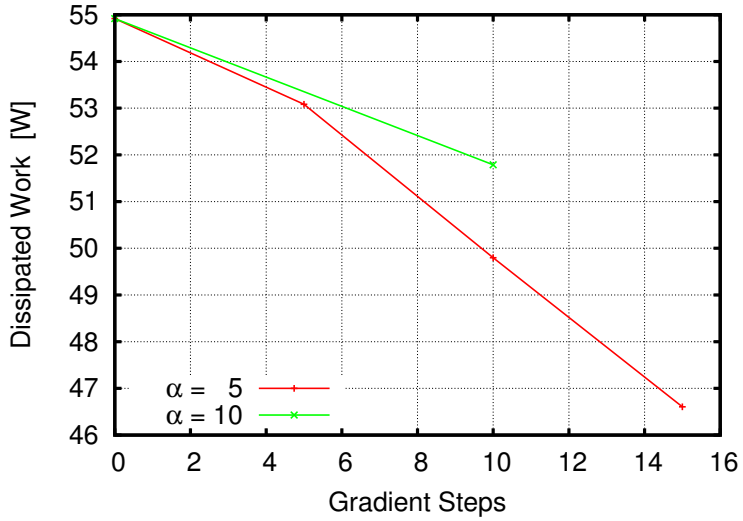

Abb. 16 Reduction of dissipated work in the blood flow due to application of different gradient stepsizes.

adjoint p-FEM solver allowing the implementation of a partitioned solution environment. Solutions of primal and adjoint FSI-problems are used to compute surface sensitivities and gradient distributions in terms of an optimization regarding a minimization in the pressure drop of the encountered fluid flow. The calculated gradient fields are then used in the context of a steepest descent algorithm leading to modifications in the shape of the considered structure approaching the optimal state of the system to be optimized. Performance and efficiency of the proposed control optimization strategy are demonstrated by the application to two examples being characteristic of ducted flow systems. The developed control algorithm provides modified geometries distinguished by significant decreases in pressure drop and smooth changes in the optimized shapes.

Literatur

1. C. Farhat K. van der Zee P. Geuzaine, Provably second-order time-accurate loosely-coupled solution algorithms for transient nonlinear computational aeroelasticity, Comput Methods Appl Mech Eng, 195:1973-2001 (2006)
2. K. Willcox J. Paduano J. Peraire, Low order aerodynamic models for aeroelastic control of turbomachines, Proc of 40th AIAA/ASME/ASCE/AHS/ASC structures, structural dynamics and materials (SDM) Conference St. Louis, USA p. 1-11 (1999)
3. A. Jameson, Optimum Aerodynamic Design Using CFD and Control Theory, AIAA-95-1729-CP (1995)
4. A. Jameson, Aerodynamic Design via Control Theory, Journal of Scientific Computing Vol. 3 No.3 (1988)
5. A. Jameson Sriram L. Martinelli, An unstructured adjoint method for transonic flows, AIAA paper, 16th AIAA CFD Conference Orlando (2003)

6. A. Jameson, Aerodynamic Shape Optimization Using the Adjoint Method, 11-14. Department of Aeronautics and Astronautics Stanford University, Von Karman Institute Brussels (2003)
7. C. Othmer, A continuous adjoint formulation for the computation of topological and surface sensitivities of ducted flows, Int. J. Numer. Meth. Fluids, 58:861-877 (2008)
8. O. Soto and R. Löhner, On The Computation of Flow Sensitivities From Boundary Integrals, 42nd AIAA Aerospace Sciences Meeting and Exhibit, Reno NV (2004)
9. A. Quarteroni G. Rozza, Optimal Control and Shape Optimization of Aorto-Coronaric Bypass Anastomoses , Mathematial Models and Methods in Applied Sciences (2003)
10. A. Lincke T. Rung, Adjoint-based Sensitivity Analysis for buoyancy-driven incompressible Navier-Stokes Equations with Heat Transfer, Proc. 8th Int. Conference Eng. Comp. Technology (2012)
11. Y. Bazilevs M.-C. Hsu and M.T. Bement, Adjoint-Based Control of Fluid-Structure Interaction for Computational Steering Applications, Procedia Computer Science, 18:1989-1998 (2013)
12. Y. Bazilevs K. Takizawa T.E. Tezduyar, Computational Fluid-Structure Interaction (Methods and Applications), Wiley (2013)
13. Y. Bazilevs V.M. Calo T.J.R. Hughes Y. Zhang, Isogeometric fluid-structure interaction: theory, algorithms, and computations, Comp. Mech., 43:3-37, Springer (2008)
14. F. Tröltzsch, Optimal Control of Partial Differential Equations: theory, methods and applications, AMS (2010)
15. J. Degroote K.J. Bathe J. Vierendeels, Performance of a new partitioned procedure versus a monolithic procedure in fluid-structure interaction, Computers and Structures 87:793-801 (2009)
16. www.openfoam.com, OpenFOAM is a registered trade mark of Silicon Graphics International Corp.
17. R. I. Issa, Solution of the implicitly discretized fluid flow equations by operator-splitting, Journal of Comp. Physics (1986)
18. A. Düster S. Hartmann E. Rank, p-FEM applied to finite isotropic hyperelastic bodies, Computer Methods in Applied Mechanics and Engineering 192:5147-5166 (2003)
19. T. Netz A. Düster S. Hartmann, High-Order finite elements compared to low-order mixed element formulations, ZAMM-Zeitschrift fuer Angewandte Mathematik und Mechanik 93:163-176 (2013)
20. M. König L. Radtke A. Düster, A flexible C++ framework for the partitioned solution of strongly coupled multifield problems, Computers & Mathematics with Applications (2016)
21. S. Brändli A. Düster, A flexible multi-physics coupling interface for partitioned solution approaches, Proc. Appl. Math. Mech. 12:363-364 (2012)
22. M. Galvez L. Badilla A. Valencia A. Zarate, Non-Newtonian blood flow dynamics in a right internal carotid artery with a saccular aneurysm, Int. Journal Num. Methods 50 (2005)
23. L. Radtke, Ein partitionierter Ansatz zur Simulation der Fluid-Struktur-Interaktion an der Schnittstelle zu künstlichen Blutgefäßen und endoluminalen Gefäßstützen, Master Thesis TU Hamburg-Harburg (2013)
24. M. Hinze et al., Optimization with PDE Constraints, Springer (2009)
25. A. Lincke T. Rung M. Hinze, An efficient line search technique and its application to adjoint topology optimization, 85th Annual Meeting Int. Association of Appl. Math. and Mech. (GAMM) (2014)